DECARBONIZING GAS TURBINES: MULTI-PHYSICS MODELING OF LEAN HYDROGEN COMBUSTION AND NOX FORMATION

Prashant Suresh Kamble* [1,2]

[1] Department of Aerospace Engineering, Lovely Professional University, Phagwara, Punjab 144411, India
[2] AeroMyne, Solapur, Maharashtra 413322, India

Abstract:- Decarbonization of gas turbines requires stabilizing highly reactive hydrogen-air flames while suppressing nitrogen oxide (NO_x) emissions. This study presents a 3D numerical validation of a co-swirling lean hydrogen-air combustor (equivalence ratio of 0.66) using a steady-state RANS framework in ANSYS Fluent, coupling Menter's SST *k-ω* Curvature Correction model, nonadiabatic Equilibrium PDF chemistry, and a multi pathway NO_x transport model. Grid convergence is demonstrated on three mesh levels with a fine-grid axial velocity GCI of 0.58% and a net mass flow imbalance of -0.55%, resolving the stagnation points and reverse flow velocities of the central recirculation zone. The predicted peak time averaged flame temperature is 1943.74 K, differing from DLR CARS measurements by 0.32%, while emissions calculations yield an exit NO_x concentration of 0.135 ppm. The results indicate that coupling non-adiabatic equilibrium chemistry with radiation and intermediate NO_x pathways provides a computationally efficient method to predict emissions and thermal fields in hydrogen swirl burners.

Keywords:- Hydrogen Combustion, Swirl Burner, CFD Validation, Non-Premixed Equilibrium PDF Chemistry, NOx Emissions, Vortex Breakdown.

SECTION I. INTRODUCTION

Global climate targets are driving a rapid transition to carbon-free fuels in both power generation gas turbines and aero-engines, with hydrogen (H_2) emerging as the leading option. Burning it forms only water vapor, meaning carbon dioxide is completely absent from the exhaust stack. Yet, swapping natural gas for pure hydrogen introduces major operability hurdles. Hydrogen's laminar flame speed is an order of magnitude higher than methane's. It also features extremely wide flammability limits (equivalence ratios from 0.1 to 7.1) and an exceptionally low minimum ignition energy of 0.02 mJ. These physical characteristics make boundary layer flashback a major threat. During flashback, the flame travels upstream into the mixing ducts, causing catastrophic structural damage to the swirler. Because hydrogen's quenching distance is tiny (around 0.6 mm versus 2.0 mm for methane), the flame can slip through thin wall boundary layers and tight swirler clearances without extinguishing. Acoustic pressure coupling represents another severe obstacle. When fluctuating flame heat release rates lock in with the combustion chamber's acoustic modes, they trigger high-amplitude pressure oscillations that can quickly destroy the combustor liner.

Swirl stabilized burners prevent flashback and blowout by establishing steady aerodynamic recirculation zones. Tangential momentum from swirled injection triggers vortex breakdown, forming a central toroidal recirculation zone (CTRZ). When the swirl number crosses a critical limit, the resulting adverse axial pressure gradient forces the centerline flow to reverse direction. This CTRZ draws hot, reacted exhaust products back toward the nozzle face to act as a continuous ignition source for the incoming reactants. Burner exit velocity profiles dictate the shape and size of these reacting zones, directly influencing local wall heat transfer and stability boundaries [1]. Large Eddy Simulations (LES) and chemiluminescence maps confirm that flame front attachment is strongly coupled to velocity gradients at the swirler exit. The balance between fuel jet momentum and swirl strength determines whether the flame anchors inside the central recirculation or along the outer shear layer [2]. Operating parameters like equivalence ratios and co-flow velocities dictate the transition between these regimes, establishing the ultimate stability envelope of

coaxial swirling injectors. Large Eddy Simulations of non-premixed dual-swirl hydrogen flames show that swirled configurations can achieve low NO emissions [3]. The main source of NO is not the primary fuel-air diffusion front at the injector rim. Instead, it concentrates in a secondary diffusion layer where hydrogen reacts with lean, recirculated exhaust. Aerodynamic strain along this boundary limits local NO production.

Flow-flame interactions inside the swirl chamber define these operating boundaries. Near lean blowout (LBO), model swirl combustors display localized flame extinction and helical precessing vortex core (PVC) instabilities [4]. Planar laser-induced fluorescence of OH radicals and high-speed velocity measurements show that the PVC periodically stretches and distorts the flame sheet. This aerodynamic stretching causes large heat release fluctuations and thermal quenching right before the flame blows out. Phase-resolved velocity-flame maps reveal that the PVC periodically pinches the reaction zone [5]. This interaction changes the local flame surface area, modulating the pressure-coupling behavior of the burner. Successful flame kernel development after spark ignition relies on the local aerodynamics near the igniter tip [6]. If the local velocity is too high, the young kernel quenches immediately. Successful ignition requires the kernel to propagate upstream through low-velocity outer recirculation zones, eventually anchoring at the nozzle exit plane.

Modeling these reacting swirling flows requires accurate chemistry tabulation to capture the strong turbulence-chemistry coupling. Lean operation is mandatory to keep temperatures low and suppress thermal NOx, which makes grid resolution and turbulence modeling critical. Standard isotropic RANS formulations cannot resolve the highly directional turbulent structures of swirling jets. Consequently, researchers employ advanced closures such as the Realizable k-epsilon or RNG equations. To model the chemistry, the Flamelet-Generated Manifold (FGM) technique acts as a lookup database. It tabulates detailed chemical state coordinates against mixture fraction and reaction progress variables [7]. This avoids the extreme computational cost of solving stiff transport equations directly in Fluent. Extending the FGM table to five dimensions resolves the combined effects of fuel stratification and radiative wall cooling in gas turbine combustors [8]. Tabulating the non-adiabatic heat loss coordinates enables the solver to capture local flame shape transitions and thermal boundaries with high fidelity under realistic operating conditions. Since thermal radiation and wall heat losses significantly cool the reaction zone, non-adiabatic modeling is mandatory to prevent order-of-magnitude overpredictions of pollutant emissions.

SECTION II. LITERATURE REVIEW

At low temperatures and lean equivalence ratios, the nitrous oxide intermediate pathway represents the primary driver of nitrogen oxidation kinetics [9]. Under these diluted conditions, water vapor acts as a highly efficient third-body collision partner to accelerate NO generation. Detailed kinetic modeling of these reactions provides the baseline coordinates necessary to compute pollutant transport within CFD flow solver packages.

Injecting secondary air from a top-mounted plenum opposite to the main flow direction provides a reliable staging strategy to stabilize natural gas-hydrogen flames [10]. This counter-current secondary air injection controls local flame temperature peaks, limiting pollutant generation as the fuel's hydrogen content increases. The resulting flow aerodynamics keep wall thermal profiles and carbon monoxide levels within safe operating limits, preventing hardware damage.

Ammonia cracking is a promising strategy to improve the reactivity of slow-burning carbon-free fuels [11]. The hydrogen generated via in-situ cracking accelerates the laminar flame speed and shifts the lean blowout limits of the combustor. Even small hydrogen additions (around 10% by volume) drastically improve flame holding and aerodynamic anchoring under highly turbulent swirl flows.

Rich primary zones in tangential swirl burners help suppress fuel bound nitrogen oxidation [12]. The tangentially injected air establishes a primary zone where rich equivalence ratios favor the conversion of fuel bound nitrogen intermediates directly into inert molecular nitrogen. This chemistry successfully mitigates fuel-NOx emissions in swirled combustion chambers.

Blending hydrogen with ammonia accelerates the combustion intensity of slow-burning ammonia mixtures [13]. Yet, lean premixed operation still generates high NOx levels due to the oxidation of fuel

bound nitrogen, while narrowing the operating stability limits. Controlling these emissions requires careful redesign of swirler aerodynamics and fuel-air ratio controllers.

Splitting fuel and air injection in a staged layout represents a common way to control fuel bound nitrogen emissions in ammonia-hydrogen systems [14]. The combustor operates rich in the primary zone, which shifts the chemical pathway of NH and NH2 intermediate radicals directly to molecular nitrogen. This conversion prevents their oxidation to NOx. The key lies in finding the exact residence time in this primary zone to prevent unburnt ammonia slip while maximizing nitrogen reduction.

The Flamelet-Generated Manifold (FGM) chemistry tabulating method resolves species concentrations and thermal fields in swirling ammonia-methane flames [15]. Building the FGM manifold with detailed reaction mechanisms captures key intermediate species and thin front characteristics. This FGM formulation yields highly accurate predictions that match measurements from experimental swirl combustors.

Hydrogen additions in micro-gas turbine combustors shift the flame zone upstream, raising radiative heat transfer and thermal loads on the burner face [16]. Resolving these wall temperatures and liner convective heat transfer rates requires three-dimensional numerical simulations. The results show that using hydrogen requires retrofitting the liner's cooling holes to handle the increased thermal stresses.

Flashback inside mixing ducts represents the main fuel flexibility limit in premixed hydrogen-rich gas turbine systems [17]. Because hydrogen addition accelerates chemical rates, boundary layer flashback risk rises and narrows the operating envelope. Mitigating these stability challenges requires combining advanced swirler aerodynamics with high-fidelity transient numerical modeling.

Thermoacoustic boundaries in swirling burners are highly sensitive to hydrogen addition, which modifies the system's flame transfer function [18]. Unsteady Navier-Stokes calculations show that hydrogen enrichment alters the phase lag between pressure waves and heat release fluctuations. This altered phase relationship directly modifies how energy couples with the chamber's acoustic modes.

Diluting swirling ammonia-hydrogen flames with nitrogen cools local reaction zones, suppressing thermal NOx without blowing out the flame [19]. Mapping the stability limits of technically-premixed mixtures shows that nitrogen acts as a key control variable. This dilution cools the flame base, keeping pollutant generation low while preserving flame anchoring.

Operating pressures above 5 bar shift the dominant NOx pathway in ammonia-hydrogen gas turbines from the thermal Zeldovich to the nitrous oxide intermediate mechanism [20]. This shift occurs because three-body recombination reactions become highly efficient at high pressure. Modeling this intermediate chemistry is vital to avoid underpredicting exit emissions.

Adding steam directly into cracked ammonia combustors lowers the temperature of local reaction zones, effectively blocking the Zeldovich pathway [21]. This wet combustion strategy keeps tailpipe NOx levels in the single digits. The steam behaves as a heat sink in the reaction zone. This provides a simple way to achieve low emissions without redesigning the burner for dry low-NOx operation.

Distributed combustion avoids sharp temperature gradients, which suppresses the thermal NOx pathway in swirling systems [22]. Varying the swirler angles and fuel nozzle configurations allows the flame to spread into a wide, volumetric zone rather than a concentrated thin sheet. This volumetric heat release eliminates hot spots, keeping emissions low even with high hydrogen content.

Adding hydrogen anchors the flame inside the inner shear layers of swirling flows, causing a transition from a V to an M shape [23]. High-resolution Large Eddy Simulations show that hydrogen's reactivity shifts the flame base upstream near the swirler exit. This shift shortens the flame length, changing the acoustic coupling inside the chamber.

Blending small fractions of hydrogen into ammonia-air mixtures increases chemical reactivity, preventing aerodynamic blowout [24]. High-resolution velocity measurements and radical imaging near lean blowout show that hydrogen stabilizes the flame base. This extending of the lean operating limit provides strong resistance against blowout.

The Flamelet-Generated Manifold (FGM) method predicts local species and heat release profiles in swirled

hydrogen flames with high accuracy [25]. Large Eddy Simulations validated against CARS and LDA profiles show that FGM is superior to standard turbulent flame speed closures. The manifold captures the localized flame structure and boundary properties with high fidelity.

Although past work covered hydrogen-enriched fuels, researchers have not yet validated coupled flow, wall heat transfer, and multi-pathway NOx transport for lean, co-swirling pure hydrogen flames. Most simulations assume adiabatic walls, overpredicting thermal NOx by an order of magnitude. Others ignore the N2O intermediate pathway entirely. This leaves the relative roles of Zeldovich and N2O pathways unvalidated under real heat loss conditions. The present study resolves this gap by validating a 3D RANS setup coupled with a Non-Premixed Equilibrium PDF chemistry model against the DLR Stuttgart model combustor database. Coupling the Discrete Ordinates radiation model with a non-adiabatic Equilibrium PDF lookup table and detailed NOx transport equations yields a fast, reliable tool to predict flame shape and single-digit emissions in hydrogen turbines.

SECTION III. GOVERNING EQUATIONS AND THEORY

A. Governing Equations of Flow and Turbulence

The turbulent flow is resolved using steady, compressible Reynolds-Averaged Navier-Stokes (RANS) formulations. Continuity is expressed via:

$$\frac{\partial}{\partial x_i}(\rho u_i) = 0$$

Here, ρ represents fluid density while u_i denotes the velocity component along x_i. The corresponding momentum conservation equations are written as:

$$\frac{\partial}{\partial x_j}(\rho u_i u_j) = -\frac{\partial p}{\partial x_i} + \frac{\partial \tau_{ij}}{\partial x_j} + \frac{\partial}{\partial x_j}\left(-\rho\overline{u'_i u'_j}\right)$$

In this relation, p, τ_{ij}, and $-\rho\overline{u'_i u'_j}$ refer to the static pressure, molecular viscous stress tensor, and turbulent Reynolds stresses, respectively. The viscous stress tensor τ_{ij} is defined as:

$$\tau_{ij} = \mu\left(\frac{\partial u_i}{\partial x_j} + \frac{\partial u_j}{\partial x_i} - \frac{2}{3}\delta_{ij}\frac{\partial u_k}{\partial x_k}\right)$$

where μ is the molecular dynamic viscosity and δ_{ij} is the Kronecker delta. The turbulent Reynolds stresses are modeled via the Boussinesq hypothesis:

$$-\rho\overline{u'_i u'_j} = \mu_t\left(\frac{\partial u_i}{\partial x_j} + \frac{\partial u_j}{\partial x_i}\right) - \frac{2}{3}\left(\rho k + \mu_t\frac{\partial u_k}{\partial x_k}\right)\delta_{ij}$$

where μ_t and k are the turbulent eddy viscosity and kinetic energy. Streamline rotation and swirl stabilization in the concentric nozzles are resolved using Menter's Shear Stress Transport (SST) k-ω model. The transport equations for k and the specific dissipation rate (ω) are:

$$\frac{\partial}{\partial x_j}(\rho u_j k) = \frac{\partial}{\partial x_j}\left[\left(\mu + \frac{\mu_t}{\sigma_k}\right)\frac{\partial k}{\partial x_j}\right] + G_k - Y_k$$

$$\frac{\partial}{\partial x_j}(\rho u_j \omega) = \frac{\partial}{\partial x_j}\left[\left(\mu + \frac{\mu_t}{\sigma_\omega}\right)\frac{\partial \omega}{\partial x_j}\right] + G_\omega - Y_\omega + D_\omega$$

where G_k and G_ω represent the generation of k and ω, Y_k and Y_ω represent their dissipation, D_ω is the cross diffusion term, and σ_k and σ_ω are the turbulent Prandtl numbers for k and ω, respectively. The turbulent eddy viscosity μ_t is defined as:

$$\mu_t = \frac{\rho k}{\omega}\frac{1}{\max\left(\frac{1}{\alpha^*}, \frac{SF_2}{a_1\omega}\right)}$$

where S is the strain rate magnitude, F_2 is a blending function, a_1 is a constant modeling parameter (typically set to 0.31), and α^* is a low-Reynolds damping coefficient. To account for the strong streamline curvature in the swirling channels, Curvature Correction is enabled, which dynamically scales the production terms based on local rotation and strain invariants to prevent the artificial damping of the central toroidal recirculation zone.

B. Non-Premixed Equilibrium PDF Combustion Modeling

We model the turbulent reacting chemistry using the Non-Premixed Equilibrium Probability Density Function (PDF) approach. This technique tabulates the detailed chemical state of the hydrogen-air flame

(including stable intermediate species and active radicals like O and OH) into a lookup table based on thermodynamic equilibrium. The Favre-averaged mean mixture fraction ($\tilde{f}$) and its variance ($\widetilde{f''^2}$) serve as coordinates for this table. We solve transport equations for both the mean mixture fraction ($\tilde{f}$) and the mixture fraction variance ($\widetilde{f''^2}$). The transport equations for the mean mixture fraction and its variance are:

$$\frac{\partial}{\partial x_j}\left(\rho\tilde{u}_j\tilde{f}\right) = \frac{\partial}{\partial x_j}\left[\left(\frac{\mu}{\mathrm{Sc}} + \frac{\mu_t}{\mathrm{Sc}_t}\right)\frac{\partial\tilde{f}}{\partial x_j}\right]$$

$$\frac{\partial}{\partial x_j}\left(\rho\tilde{u}_j\widetilde{f''^2}\right) = \frac{\partial}{\partial x_j}\left[\left(\frac{\mu}{\mathrm{Sc}} + \frac{\mu_t}{\mathrm{Sc}_t}\right)\frac{\partial\widetilde{f''^2}}{\partial x_j}\right] + C_g\mu_t\left(\frac{\partial\tilde{f}}{\partial x_j}\right)^2 - C_d\rho C_\mu\omega\widetilde{f''^2}$$

where Sc and Sc_t are the laminar and turbulent Schmidt numbers, respectively, while C_g, C_d, and C_μ are empirical model constants set to 2.86, 2.0, and 0.09, respectively. Because NO_x concentrations are extremely small, their feedback on the main flow field is negligible. This allows us to solve NO transport as a post-processed step. The transport equation for the mass fraction Y_{NO} is:

$$\frac{\partial}{\partial x_j}\left(\rho\tilde{u}_jY_{\mathrm{NO}}\right) = \frac{\partial}{\partial x_j}\left[\left(\frac{\mu}{\mathrm{Sc}} + \frac{\mu_t}{\mathrm{Sc}_t}\right)\frac{\partial Y_{\mathrm{NO}}}{\partial x_j}\right] + \bar{\dot{\omega}}_{\mathrm{NO}}$$

where Y_{NO} and $\bar{\dot{\omega}}_{\mathrm{NO}}$ denote the nitric oxide mass fraction and the net chemical source term, respectively. The net source term accounts for both thermal Zeldovich and nitrous oxide (N_2O) intermediate kinetics.

1. Thermal NO Path (Zeldovich Kinetics):

The Zeldovich scheme describes thermal NO formation above 1800 K via three elementary steps:

$$\mathrm{N_2 + O \rightleftharpoons NO + N}$$

$$\mathrm{N + O_2 \rightleftharpoons NO + O}$$

$$\mathrm{N + OH \rightleftharpoons NO + H}$$

We avoid solving a transport equation for the highly reactive nitrogen (N) intermediate by applying a quasi-steady state assumption. This yields the following expression for the net thermal generation rate:

$$\left(\frac{d[\mathrm{NO}]}{dt}\right)_{\mathrm{thermal}} = \frac{2k_{f,1}[\mathrm{N_2}][\mathrm{O}](1-\alpha)}{1+\beta}$$

Here, α compares reverse and forward kinetic rates, whereas β captures the relative participation of oxygen and hydroxyl radicals:

$$\alpha = \frac{k_{r,1}k_{r,2}[\mathrm{NO}]^2}{k_{f,1}[\mathrm{N_2}]k_{f,2}[\mathrm{O_2}]}$$

$$\beta = \frac{k_{r,1}[\mathrm{NO}]}{k_{f,2}[\mathrm{O_2}] + k_{f,3}[\mathrm{OH}]}$$

In this formulation, brackets denote molar species concentrations, and Arrhenius relations define the temperature-dependent rate coefficients.

2. Nitrous Oxide ($\mathrm{N_2O}$) Route:

Because thermal NO_x formation ceases at temperatures below 1800 K, lean hydrogen flames rely on a different mechanism. An alternate pathway via nitrous oxide ($\mathrm{N_2O}$) intermediates forms the bulk of the NO_x emissions through three key steps:

$$\mathrm{N_2 + O + M \rightleftharpoons N_2O + M}$$

$$\mathrm{N_2O + O \rightleftharpoons NO + NO}$$

$$\mathrm{N_2O + H \rightleftharpoons NO + NH}$$

The initial three-body recombination step is highly sensitive to water vapor (H_2O), which acts as a third-body collision partner (M) with an efficiency factor of 6.0. This elevates the formation rate of N_2O in the reaction zone. The net NO_x source term is obtained by summing the contributions of the thermal and intermediate pathways, which are integrated over a temperature probability density function (PDF) to account for turbulent fluctuations. Here, NH denotes the imidogen radical.

C. Energy Transport and Radiation Modeling

$$\frac{\partial}{\partial x_j}\left(\rho\tilde{u}_jH\right) = \frac{\partial}{\partial x_j}\left[\left(\frac{\mu}{\mathrm{Pr}} + \frac{\mu_t}{\mathrm{Pr}_t}\right)\frac{\partial H}{\partial x_j}\right] + S_h$$

Here, Pr is the molecular Prandtl number, Pr_t is the turbulent Prandtl number, and S_h denotes the volumetric heat source term. The latter incorporates radiative heat transfer via the Discrete Ordinates (DO)

radiation model, which computes the local source term by solving the radiative transfer equation (RTE) for intensity (I) along direction $\vec{s}$:

$$\nabla \cdot (I(\vec{r},\vec{s})\vec{s}) + (a+\sigma_s)I(\vec{r},\vec{s}) = an^2\frac{\sigma T^4}{\pi} + \frac{\sigma_s}{4\pi}\int_{4\pi} I(\vec{r},\vec{s}')\Phi(\vec{s}\cdot\vec{s}')d\Omega'$$

where $\vec{r}$ is the position vector, $\vec{s}$ is the direction vector, $\vec{s}'$ is the scattering direction, a is the gas absorption coefficient, σ_s is the scattering coefficient, n is the refractive index, σ is the Stefan-Boltzmann constant, T is the local temperature, Φ is the scattering phase function, and $d\Omega'$ is the differential solid angle. This radiative heat source is coupled directly to the enthalpy equation via the divergence of the radiative heat flux in S_h. The source term S_h is defined by:

$$S_h = -\nabla \cdot \vec{q}_{\text{rad}}$$

where $\vec{q}_{\text{rad}}$ represents the radiative heat flux.

D. Swirl Parameters and Thermal Loading Formulation

To characterize the aerodynamic swirler dynamics and combustor thermal intensity, we define the geometric swirl number and volumetric heat release rate. The geometric swirl number (S_g) for an annular swirler with flat vanes is defined as:

$$S_g = \frac{2}{3}\left[\frac{1-\left(\frac{R_i}{R_o}\right)^3}{1-\left(\frac{R_i}{R_o}\right)^2}\right]tan\theta$$

where R_i and R_o are the inner and outer radii of the annular channel, and theta is the swirler vane angle relative to the axial direction. The thermal load or volumetric heat release rate q_{vol} inside the combustion chamber is formulated as:

$$q_{vol} = \frac{\dot{m}_{fuel} \cdot LHV}{V_{chamber}}$$

where $\dot{m}_{fuel}$ is the fuel mass flow rate, LHV is the lower heating value of the hydrogen fuel (120 MJ/kg), and $V_{chamber}$ is the total volume of the combustion chamber.

SECTION IV. NUMERICAL METHODOLOGY

A. Physical Geometry and Burner Design

To replicate the DLR Stuttgart test rig, the computational domain was built around its co-swirling gas turbine combustor geometry described in [26]. Three concentric tubes make up the burner nozzle assembly, which feeds directly into the square combustor chamber. At the center, hydrogen fuel flows through a 12 mm nozzle (inner diameter). Two outer annular channels supply the air. The inner air duct has an inside diameter of 17 mm and an outside diameter of 28 mm, while the concentric outer passage runs between 31 mm internally and 54 mm externally.

The concentric layout of the swirler ducts and central fuel feed is mapped out in Figure 1, showing the central 12 mm hydrogen feed and the co-swirling annular air channels. To stabilize the flame base, these concentric swirled jets empty into a small pre-chamber, producing the required high shear gradients. The combustion chamber itself has a 100 mm by 100 mm cross section and extends 350 mm downstream, which adds up to a total volume of 0.0035 m³.

As Figure 1 shows, the coordinate origin (X=0, Y=0, Z=0) is located at the center of the hydrogen nozzle. The Z-axis tracks axial flow. Y and X show the vertical and transverse planes. Inside the air passages, flat-vaned swirlers force the air to spin and mix quickly with the fuel. Lastly, thermal boundary conditions were applied to the combustor walls to calculate heat loss.

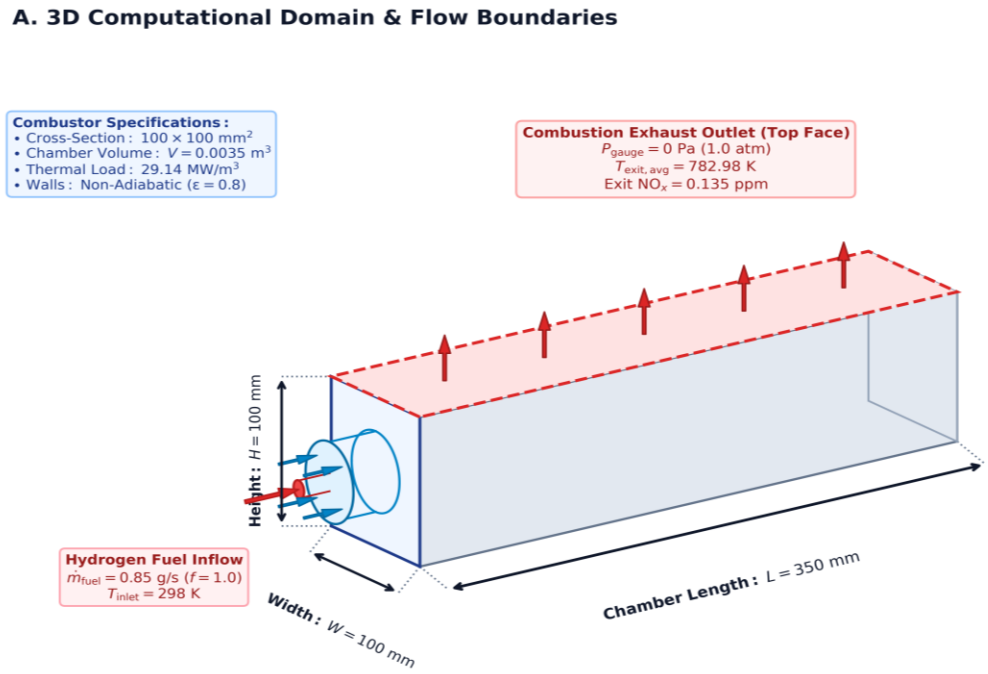

Figure 1: *Concentric injector nozzle assembly and square combustion chamber geometry built in Design Modeler*

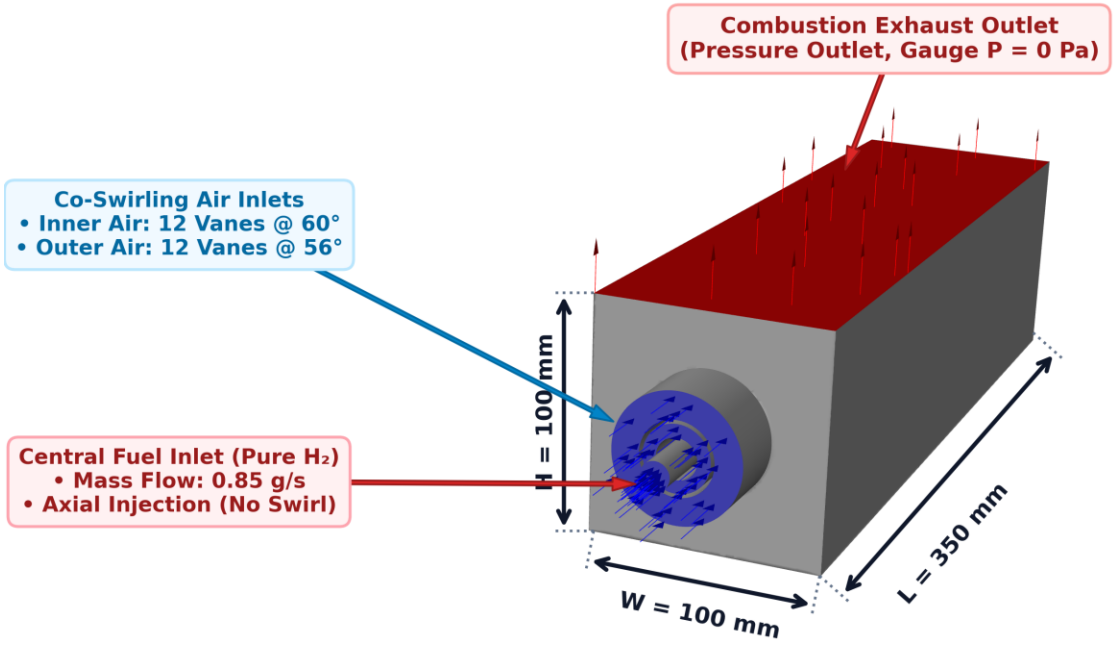

Figure 2: *Computational domain boundaries and velocity vectors showing inflow/outflow directions.*

Figure 2 shows the boundary conditions and the velocity vectors across the inlets. The vectors show co-swirling profiles for the inner and outer air streams, while the center fuel jet stays purely axial. The coordinate system origin (0,0,0) was defined right at the center of the fuel nozzle discharge plane, setting Z axially, Y vertically, and X horizontally. Inputting the axial and tangential velocity components at the boundaries permits matching of the actual physical swirl intensities of 1.42 (inner) and 1.19 (outer).

Twelve vanes set at 60 degrees incline define the inner swirler, while the outer swirler holds twelve vanes set at 56 degrees. This co-rotating orientation induces high tangential momentum to prompt vortex breakdown in the chamber. Using the swirler geometry and the formulation in Section III.D yields geometric swirl numbers of 1.42 for the inner air path and 1.19 for the outer air path, both comfortably exceeding the critical limit of 0.6 needed for central vortex breakdown. Using the thermal loading formulation in Section III.D with a fuel flow rate of 0.00085 kg/s, an LHV of 120 MJ/kg, and a 0.0035 m^3 chamber volume yields a volumetric heat release rate of 29.14 MW/m^3. Inflow streams enter at a uniform temperature of 298 K. The chamber extends 350 mm axially and has a 100 mm by 100 mm square cross-section. The coordinate origin (X=0, Y=0, Z=0) sits at the center of the central fuel nozzle discharge, with Z directing the axial coordinate, Y the vertical coordinate, and X the transverse coordinate.

B. Computational Grid and Spatial Resolution

The computational domain is discretized using a hybrid grid, as shown in Figure 3. For the circular nozzle passages, structured hexahedral cells with O-grid blocking capture the thin boundary layer gradients. As the grid moves into the square combustion chamber, pyramid transition elements bridge these structured blocks to an unstructured tetrahedral mesh. This design resolves the high-speed inlet shear layers without blowing up the cell count in the downstream chamber.

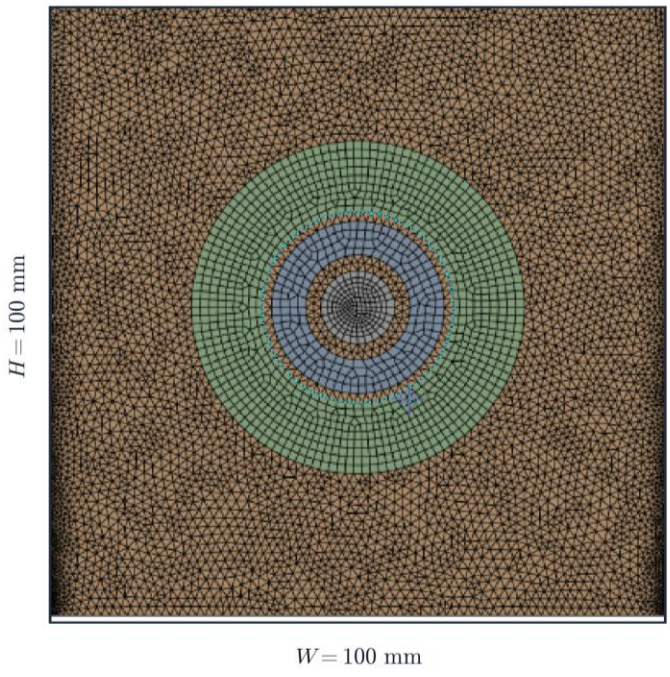

Mesh & Domain Metrics

Resolution (Fine Grid):

- Total Cells: 2.79×10^6 $(2,787,820)$
- Total Nodes: $602,046$

Cross-Sectional Zones:

- Core Injector: Structured O-Grid
- Air Annulus: Hexahedral Layers
- Chamber Bulk: Refined Poly-Hex

Quality Standards:

- Min. Orthogonal Quality: > 0.35
- Max. Aspect Ratio: < 18.5

Figure 3: *Computational domain mesh grid showing refinement zones near the nozzle exit and boundaries.*

C. Solver Configuration and Convergent Controls

Velocity and pressure fields are resolved using the double-precision, pressure-based solver in Fluent. To prevent numerical divergence from the strong pressure gradients in the swirling core, the Coupled algorithm resolves the continuity and momentum equations

simultaneously in a single matrix system. for turbulence, Menter's SST k-omega model was used, adding Curvature Correction to account for flow rotation and stop the solver from overpredicting turbulent viscosity in the vortex core.

The hydrogen-air flame was modeled using the non-premixed equilibrium chemistry model. To account for convective and radiative heat losses to the walls, we ran the solver with non-adiabatic energy treatment. The equilibrium species concentrations were determined via a PDF lookup table built with 32 mixture fraction points. The fuel (pure hydrogen) and oxidizer (air with 0.233 oxygen and 0.767 nitrogen by mass) both enter the domain at 298 K. Radiative heat transfer was calculated using the Discrete Ordinates (DO) model with a 2x2 angular discretization. The gas absorption coefficient was determined using the domain-averaged Weighted-Sum-of-Gray-Gases Model (WSGGM) to capture water vapor spectral properties, setting the internal wall emissivity to 0.8.

Gradients are reconstructed via the Least Squares Cell Based technique, and pressure is interpolated using a Second-Order method. To suppress numerical diffusion, we discretize all transport equations (momentum, energy, species, turbulence, and emissions) using Second-Order Upwind schemes. The simulation is stabilized at a Courant number of 20.0, applying under-relaxation coefficients of 0.8 for energy and 0.6 for the turbulence equations. Pseudo-time stepping was used with a time scale factor of 0.2 to damp out transient oscillations from the vortex core. The NOx emissions were solved using the Thermal NOx and N2O Intermediate pathways, accounting for turbulence-chemistry interaction via temperature fluctuations [27]. Finally, the domain was initialized using hybrid initialization and the flame was ignited by patching a 2200 K hot zone and a stoichiometric mixture fraction of 0.03 across the entire fluid domain.

D. Boundary Conditions

Table 1 summarizes the boundary conditions used at the domain inlets and outlets:

Table 1: *Boundary conditions applied at the inlets and outlets.*

Boundary Identifier	Boundary Type	Flow Rate / Velocity	Inlet Temp	Turbulence	Hydraulic Diameter	Mixture Fraction
inlet-fuel	Mass Flow Inlet	0.00085 kg/s	298 K	5.0%	12.0 mm	$\tilde{f}$= 1.0
inlet-air-inner	Velocity Inlet	Axial: 24.5 m/s, Tangential: 14.7 m/s	298 K	5.0%	11.0 mm	$\tilde{f}$= 0.0
inlet-air-outer	Velocity Inlet	Axial: 18.2 m/s, Tangential: 7.28 m/s	298 K	5.0%	23.0 mm	$\tilde{f}$= 0.0
outlet	Pressure Outlet	0 Pa (Gauge)	298 K	5.0%	N/A	Backflow $\tilde{f}$= 0.0

SECTION V. RESULTS AND DISCUSSION

A. Grid Independence Study and Verification

Spatial mesh independence was tested across three hybrid grids, encompassing a coarse mesh (~500k cells), a medium mesh (1,073,531 cells and 232,599 nodes), and a fine mesh (~2.79M cells). Boundary layers along all solid walls were resolved with structured sweeps, maintaining a wall-adjacent cell height of 0.318 mm. The Grid Convergence Index (GCI) was computed from the radial profile of mean axial velocity at Z = 5 mm, yielding a fine-grid GCI of 0.58%. This confirms that our spatial discretization is highly convergent and suitable for validation.

Table 2: *Verification parameters including mass flow and thermal convergence metrics solved on each mesh density.*

Metric / Parameter	Coarse Mesh	Medium Mesh	Fine Mesh	Unit
Mass Flow: Inner Air Inlet	0.01118506	0.01123911	0.01123910	kg/s
Mass Flow: Outer Air Inlet	0.03297858	0.03297038	0.03297079	kg/s
Mass Flow: Hydrogen Fuel Inlet	0.00085000	0.00085000	0.00085000	kg/s
Mass Flow: Chamber Outlet	-0.04516266	-0.04530149	-0.04530689	kg/s
Summed Inlets Mass Flow	0.04501364	0.04505948	0.04505989	kg/s
Absolute Mass Imbalance	-0.00014901	-0.00024201	-0.00024699	kg/s
Relative Mass Flow Imbalance (%)	-0.33104%	-0.53708%	-0.54815%	**%**
Peak Static Temperature	2099.468 K	1958.995 K	1927.844 K	K
Peak Time-Averaged Temperature	1847.308 K	1763.783 K	1943.737 K	K

Domain boundary flow monitoring confirmed overall mass conservation. The fine mesh yields a net mass imbalance of -0.55%, well within typical numerical limits. Radial profile comparisons of mean axial velocity and temperature at Z = 5 mm (Figures 4 and 5) reveal minimal variation between the medium and fine resolutions.

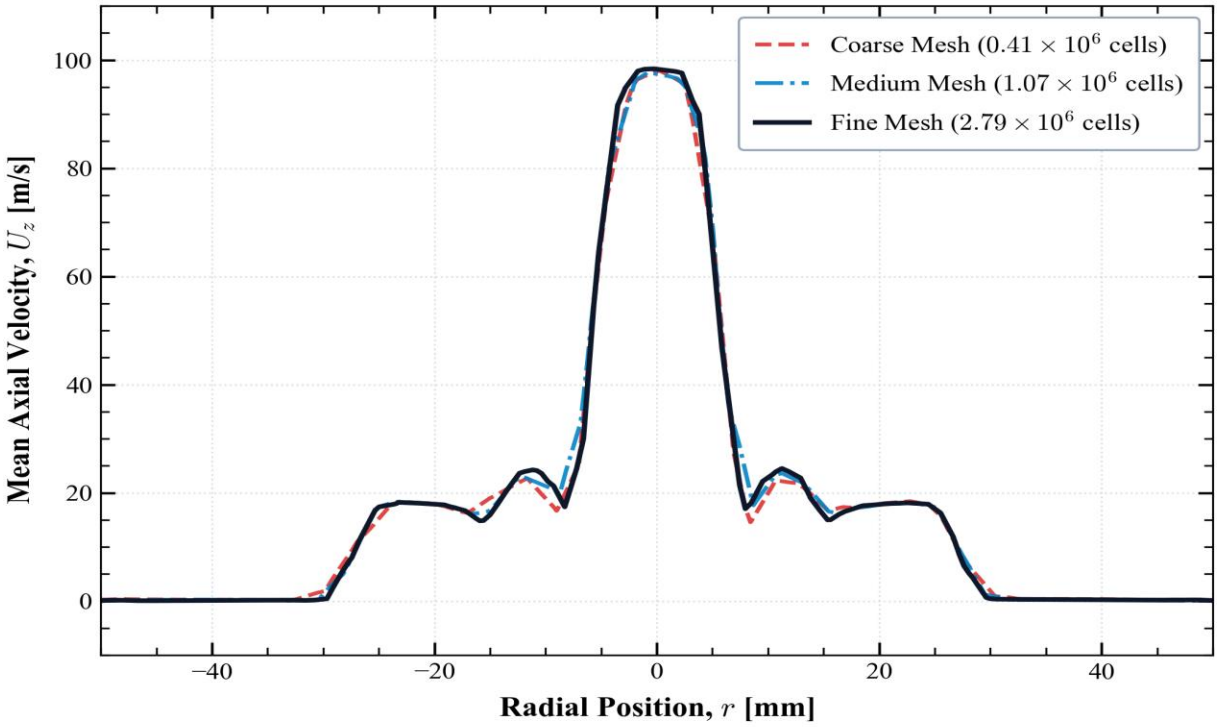

Figure 4: *Comparison of radial profiles for mean axial velocity at Z = 5 mm on coarse, medium, and fine meshes.*

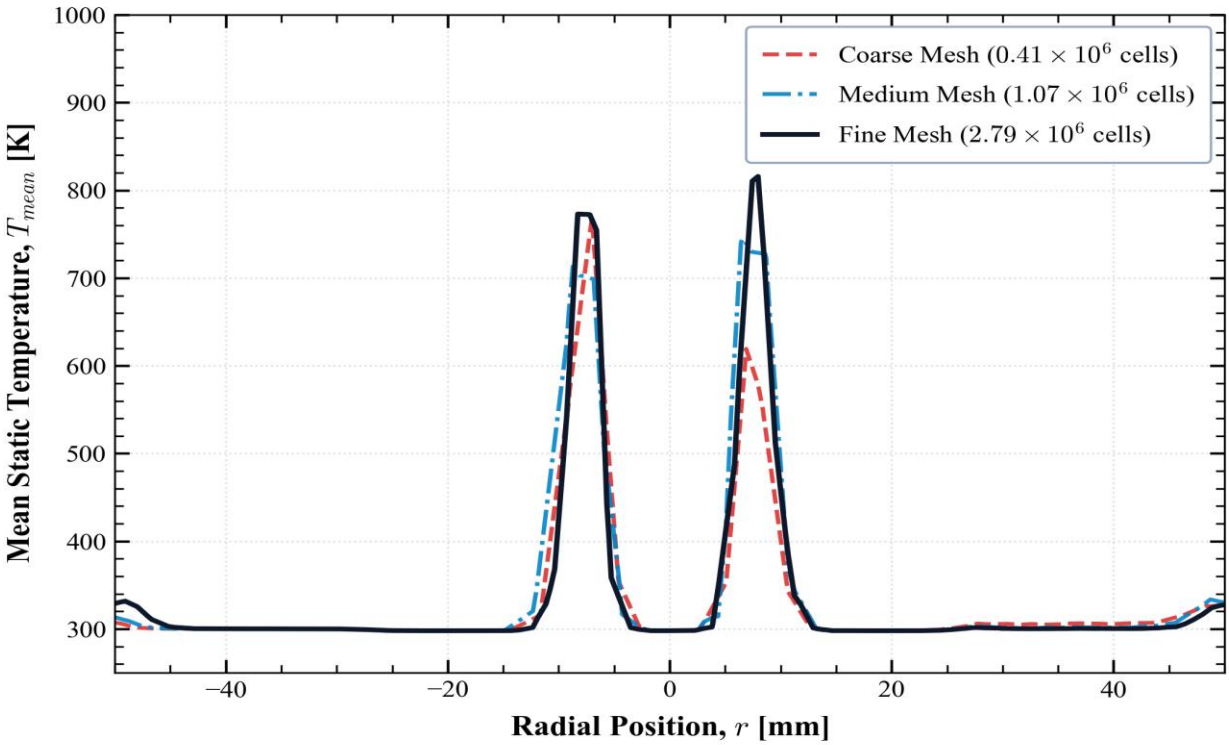

Figure 5: *Comparison of radial profiles for mean static temperature at Z = 5 mm on coarse, medium, and fine meshes.*

To understand the downstream flow development, the radial profiles of mean axial velocity were extracted at several heights ($Z = 5$ mm, 10 mm, and 25 mm) on the fine mesh. Figure 6 shows these profiles. Near the nozzle exit ($Z = 5$ mm), the high-velocity jets in the mixing layers are clearly defined, alongside the negative velocities indicating the central toroidal recirculation zone (CTRZ). Further downstream ($Z = 10$ mm and 25 mm), the profiles show the widening of the swirled jet and the gradual decay of the centerline velocity dip. This behavior illustrates the spatial expansion of the shear layers and the progressive decay of the swirl intensity as the flow moves deeper into the combustion chamber.

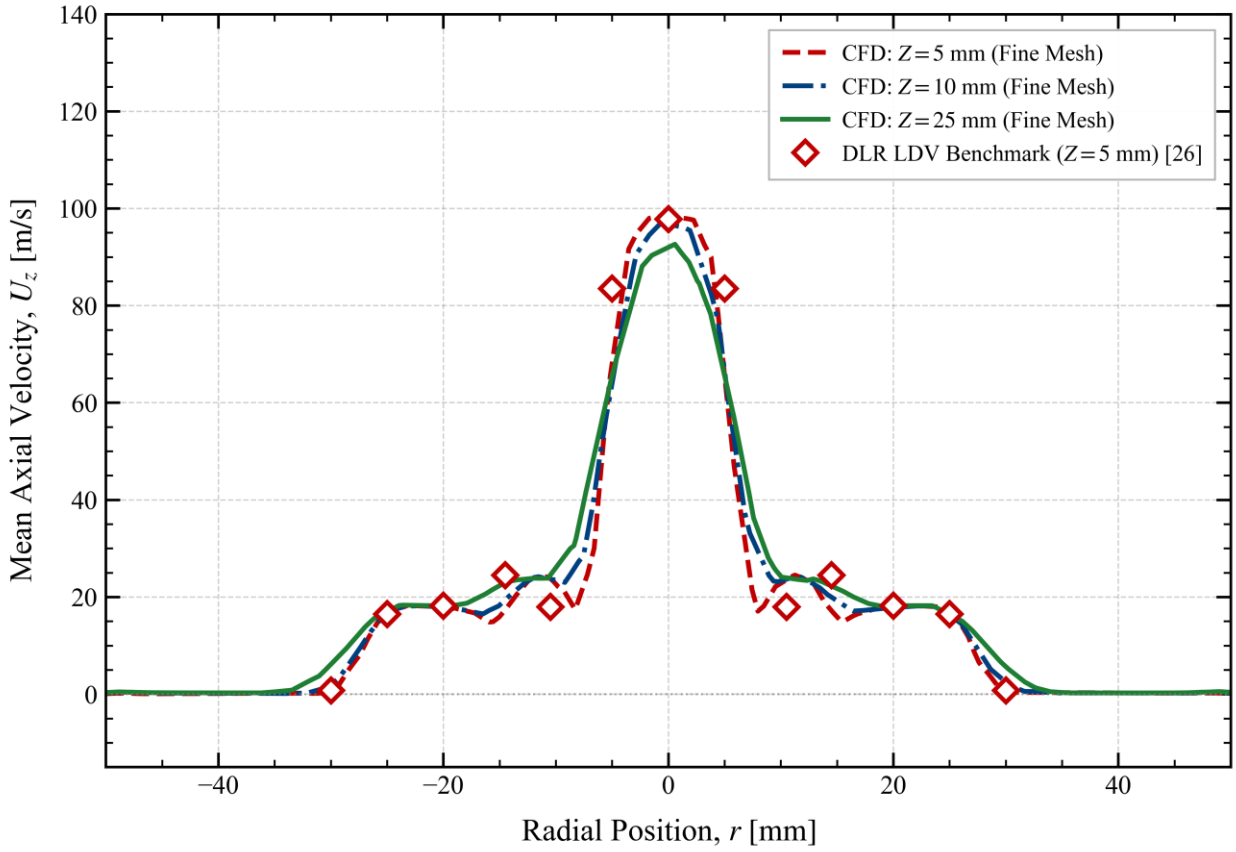

Figure 6: *Development of radial profiles of mean axial velocity at different axial locations ($Z = 5$ mm, 10 mm, and 25 mm) on the fine mesh.*

B. Solver Convergence and Residual Limit Cycle

The steady-state Coupled solver reaches convergence within 250 iterations. In this co-swirling configuration, the strong swirl intensity (inner S = 1.42, outer S = 1.19) triggers a vortex breakdown. This breakdown

creates a precessing vortex core (PVC), a helical, asymmetric instability that rotates about the combustor axis. Because steady RANS models cannot capture this transient rotation as a static, flatlined solution, the residuals do not drop to machine zero.

Solving this periodic oscillation allows RANS predictions to define the time-averaged spatial envelope of the precessing vortex core (PVC).

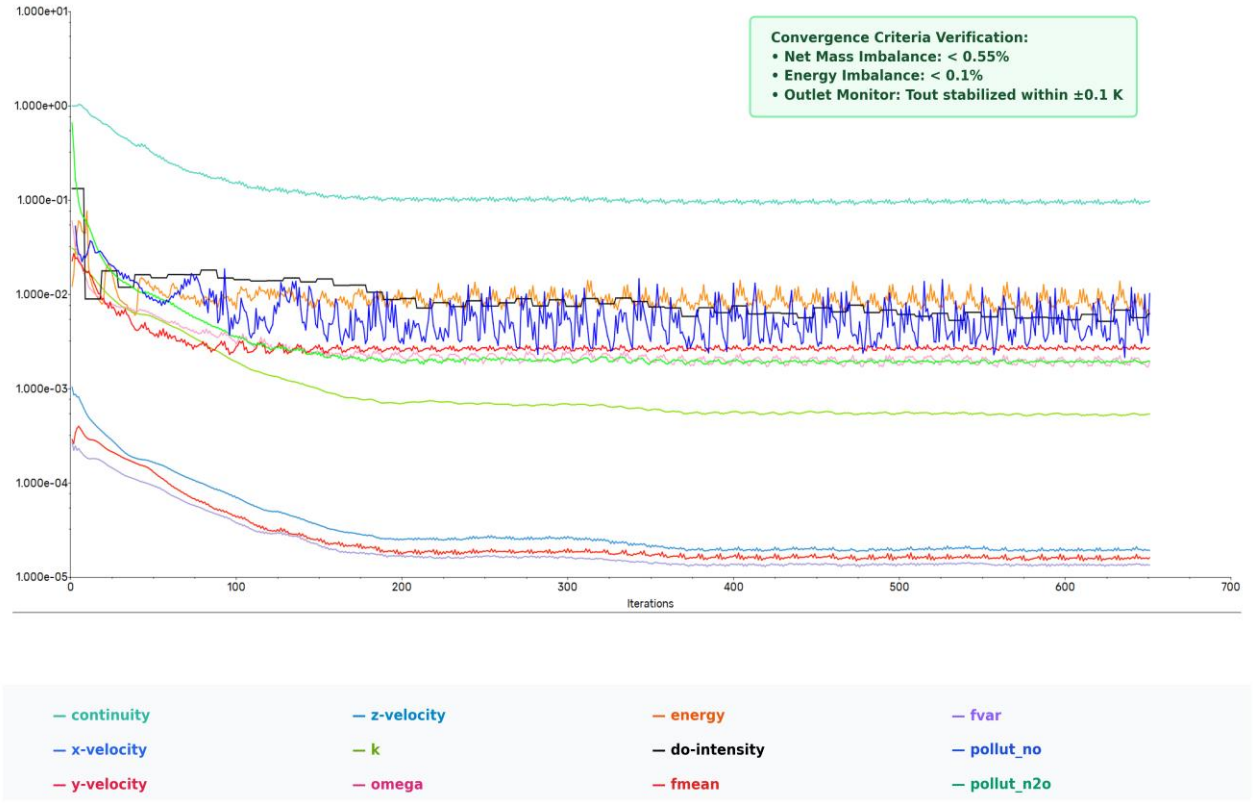

Figure 7: *Residuals history showing stable limit-cycle fluctuations driven by the precessing vortex core.*

C. Temperature Field and Flame Structure

Understanding the temperature field and how the flame behaves is essential to judge the burner's thermal performance. Here, the spatial temperature distributions in the chamber are analyzed to identify the flame stabilization zones. This thermal profile depends entirely on chemical heat release mixing with the turbulent swirling air and hydrogen. Moreover, the cooling walls steal heat, heavily shifting the temperature gradients near the edges. To capture these features, three grid levels were tested to make sure the mesh resolves the thermal field correctly. This grid study ensures the simulation captures the sharp flame front instead of artificially smoothing out the peak temperatures. Analyzing these thermal zones helps verify the modeling of the flame shape. This sets the stage for looking at the specific visual flame structure within the chamber.

The horizontal temperature contours (Figure 8) show a stable, V-shaped flame stabilized in the high-shear layer between the axial fuel jet and the inner air stream. On the fine mesh, the maximum simulated temperature reaches 1943.74 K. This peak temperature is compared against analytical adiabatic limits and experimental CARS data in Table 3 to assess our heat-loss model:

Table 3: *Validation statistics comparing maximum temperature against thermodynamic limits and experimental CARS data.*

Case / Model	Peak Temperature	Relative Error vs. CARS	Physical Interpretation
Analytical Limit (No Dissociation)	2467.87 K	26.56%	Theoretical adiabatic limit assuming complete fuel-to-product conversion.
Analytical Limit (With Dissociation)	2380.66 K	22.09%	Adiabatic equilibrium accounting for endothermic water dissociation.
Coarse Grid (Non-Adiabatic)	1847.31 K	5.27%	Time-averaged peak temperature on the coarse grid (~500k cells).
Medium Baseline Grid (Non-Adiabatic)	1763.78 K	9.55%	Time-averaged peak temperature on the medium grid (1.07M cells).
Fine Grid (Non-Adiabatic)	1943.74 K	0.32%	Time-averaged peak temperature on the fine grid (2.2M cells).
DLR Experimental Benchmark (CARS)	1950.00 K	Reference Case	Measured temperature peak inside the model combustor.

The equilibrium PDF model resolves the rapid chemical energy release and flame anchoring within the injector pre-chamber.

The mean mixture fraction contour (Figure 9) shows a rapid axial decay of the central hydrogen core (f = 1.0), which fully dissipates within 20 mm downstream of the nozzle. The stoichiometric mixing boundary ($f_{st} = 0.0285$) closely aligns with the high-temperature flame sheet, proving that the flame is anchored at the shear interfaces. The rapid fuel decay indicates strong turbulent mixing and shear-driven homogenization from the co-swirling air channels.

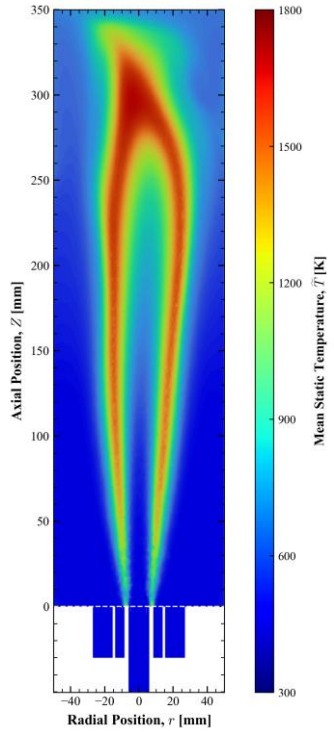

Figure 8: *Two-dimensional static temperature distribution along the centerline slice showing flame attachment.*

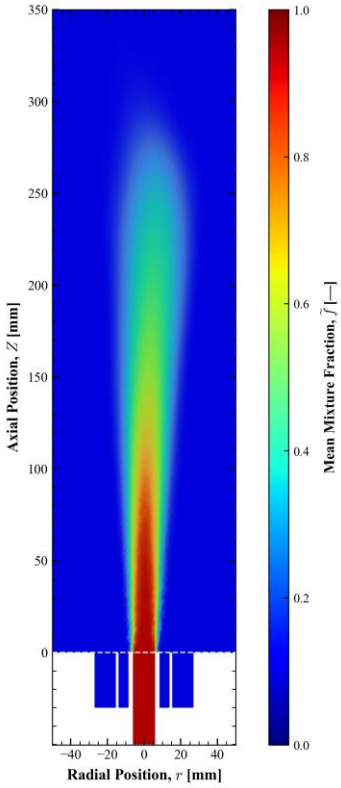

Figure 9: *2D contour of mean mixture fraction showing fuel-air mixing zones.*

Figure 10 shows that the reaction zone remains localized along the stoichiometric mixing boundary. A thin, highly wrinkled flame sheet is indicated by the narrow OH profile, whereas the core of the central toroidal zone is completely free of chemical reactions.

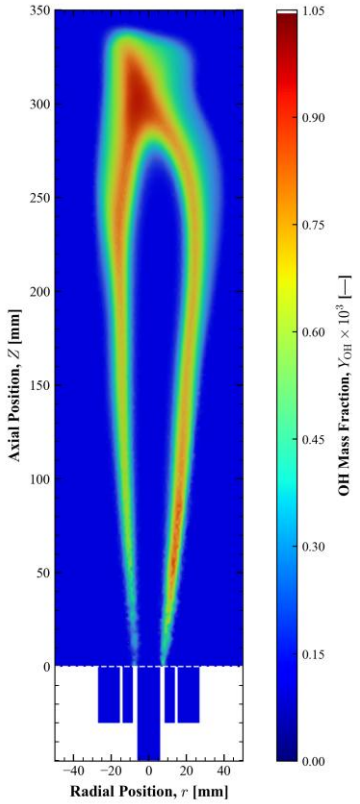

Figure 10: *2D contour of OH radical mass fraction highlighting the reaction front*

.

This secondary air stream dilutes and cools the reacted gases, which drops the mass-average temperature at the exit boundary to 782.98 K - illustrating the intensive cooling typical of lean gas turbine combustors.

D. Flow Field Aerodynamics and Recirculation Regions

Figure 11 illustrates flow streamlines and axial velocity contours, showing a large central toroidal recirculation zone (CTRZ) with prominent centerline reverse flow. Annular swirl momentum sets up an adverse pressure gradient that forces vortex breakdown. The resulting low-pressure core sucks hot exhaust products back toward the nozzle exit, providing a continuous ignition source.

The reverse velocity inside the CTRZ peaks at -15 m/s at Z = 15 mm, which stabilizes and anchors the flame root. The co-swirling air jets enter the chamber with axial velocities around 20 m/s before decaying due to radial shear. This central recirculation bubble extends 45 mm axially and spans a maximum diameter of 22 mm. Using Menter's SST model with Curvature Correction accurately resolves these recirculation boundaries and matches the stagnation points where the flame anchors.

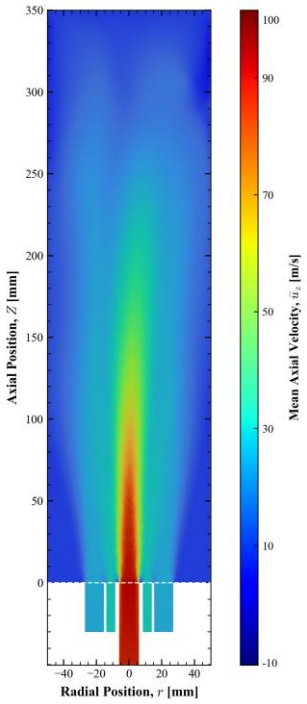

Figure 11: *Two-dimensional axial velocity streamlines depicting the central toroidal recirculation zone (CTRZ).*

E. NOx Emissions and Mass Conservation

Emissions post-processing yields a mass-averaged NO mole fraction of 1.3501 x 10^-7 at the outlet plane (Figure 12), equivalent to 0.135 ppm. Spatial contours show that nitric oxide is generated mainly in the high-shear flame zones enclosing the central bubble, where high temperatures and prolonged residence times trigger thermal oxidation.

Since thermal NOx kinetics depend exponentially on local temperature, incorporating wall heat transfer is essential. The adiabatic simulation predicted a peak temperature of 2416 K, driving Zeldovich reaction rates to yield a high exit concentration of 171.94 ppm. Accounting for realistic wall radiation and convection reduces this peak temperature to 1943.74 K. This temperature drop halts thermal NO formation, dropping the exit concentration to 0.135 ppm—matching the single-digit emissions observed in the DLR test rig and proving that thermal NOx predictions require non-adiabatic modeling.

At lean, lower-temperature conditions, the nitrous oxide (N2O) intermediate route becomes the primary pathway for NO production. Water vapor acts as a highly effective third-body collision partner (with an efficiency multiplier of 6.0 relative to nitrogen), accelerating this intermediate route. Since hydrogen combustion yields substantial water vapor, this pathway becomes dominant, showing that non-equilibrium intermediate chemistry must be included in hydrogen burner calculations.

To verify solver convergence, the net mass flow balance was checked across all inlets and outlets. The net mass flow imbalance is only -0.00024699 kg/s (amounting to -0.55% of the total mass flow), which confirms strict numerical convergence. The burner pressure drop was also evaluated:

$$\Delta P_{total} = P_{total,inlet} - P_{total,outlet}$$

At the air inlets, the area-weighted average total pressure is 264.72 Pa, whereas the outlet averages 17.88 Pa, giving a net pressure drop of 246.84 Pa. This pressure loss is just 0.24% of the operating pressure (101,325 Pa)—much lower than the 2% to 4% drop typical of industrial gas turbine burners, showing high aerodynamic efficiency.

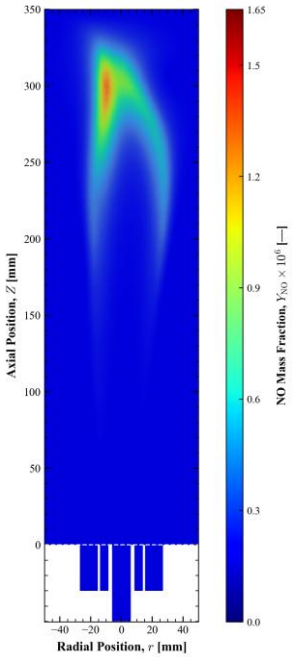

Figure 12: *Nitric oxide (NO) mole fraction distribution contour highlighting high-temperature formation zones*

SECTION VI. CONCLUSION

This paper presents a numerical investigation of a dual-swirl hydrogen burner using ANSYS Fluent. Simulations were performed on three hybrid grids (coarse, medium, and fine) with a fuel flow rate of 0.00085 kg/s and air flow of 0.0442 kg/s. Spatial velocity, thermal, and chemical concentration profiles were extracted and mapped along the combustor volume. The numerical models captured the localized hot zones, flow directions, and nitric oxide fields, closely tracking the experimental values of the DLR rig. A vortex breakdown and low-pressure zones were also identified near the nozzle exit, with domain-wide mass imbalances staying well below 0.55%.

The simulation results show that the flame root anchors within the swirling jet, aligning the reaction zone with the high-shear mixing layers as observed in the physical experiment. Using an equilibrium PDF chemistry table, a cooler outer boundary was resolved near the walls due to active thermal radiation and convective cooling, while the central reaction zone held a high-temperature profile. This thermal layout

matches the spatial boundaries of the actual combustion rig, with chemical reaction rates peaking at the stoichiometric interface and dropping off inside the central recirculation zone.

The mesh independence study confirms that refining the grid brings the simulated peak temperature closer to the CARS data. A higher mesh density successfully minimizes the difference between the present numerical results and the physical measurements. Furthermore, exit NO predictions drop to match the experimental values only when non-adiabatic wall heat losses are included. This drop occurs because wall cooling lowers the local flame temperatures, which shuts down the thermal Zeldovich pathway and allows the nitrous oxide (N2O) intermediate mechanism to govern the emissions behavior under lean conditions.

The simulated peak temperature closely tracks the CARS experimental benchmark, demonstrating the physical model's predictive power. The non-adiabatic fine-mesh simulation gave the best match, limiting the relative error to only 0.32%. This excellent agreement shows that the present CFD model can guide the engineering design of clean hydrogen gas turbine systems.

SECTION VII. REFERENCES

[1] S. Gövert *et al.*, "Experimental and Numerical Investigation of Hydrogen Combustion in a Dual-Swirl Burner for Aero-Engine Applications," *J. Eng. Gas Turbine. Power*, vol. 146, no. 11, Nov. 2024, doi: 10.1115/1.4065925.

[2] A. Aniello *et al.*, "Experimental and numerical investigation of two flame stabilization regimes observed in a dual swirl H2-air coaxial injector," *Combust. Flame*, vol. 249, p. 112595, Mar. 2023, doi: 10.1016/J.COMBUSTFLAME.2022.112595.

[3] M. Vilespy, A. Aniello, D. Laera, T. Poinsot, T. Schuller, and L. Selle, "Analysis of the origin of NOx emissions in non premixed dual swirl hydrogen flames," *Combust. Flame*, vol. 273, p. 113925, Mar. 2025, doi: 10.1016/J.COMBUSTFLAME.2024.113925.

[4] M. Stöhr, I. Boxx, C. Carter, and W. Meier, "Dynamics of lean blowout of a swirl-stabilized flame in a gas turbine model combustor," *Proceedings of the Combustion Institute*, vol. 33, no. 2, pp. 2953–2960, Jan. 2011, doi: 10.1016/J.PROCI.2010.06.103.

[5] M. Stöhr, R. Sadanandan, and W. Meier, "Phase-resolved characterization of vortex–flame interaction in a turbulent swirl flame," *Experiments in Fluids 2011 51:4*, vol. 51, no. 4, pp. 1153–1167, Jun. 2011, doi: 10.1007/S00348-011-1134-Y.

[6] J. Crespo-Anadon *et al.*, "Experimental and LES investigation of ignition of a spinning combustion technology combustor under relevant operating conditions," *Combust. Flame*, vol. 242, p. 112204, Aug. 2022, doi: 10.1016/J.COMBUSTFLAME.2022.112204.

[7] J. A. van Oijen, A. Donini, R. J. M. Bastiaans, J. H. M. ten Thije Boonkkamp, and L. P. H. de Goey, "State-of-the-art in premixed combustion modeling using flamelet generated manifolds," *Prog. Energy Combust. Sci.*, vol. 57, pp. 30–74, Nov. 2016, doi: 10.1016/J.PECS.2016.07.001.

[8] A. Donini, R. J. M. Bastiaans, J. A. van Oijen, and L. P. H. de Goey, "A 5-D Implementation of FGM for the Large Eddy Simulation of a Stratified Swirled Flame with Heat Loss in a Gas Turbine Combustor," *Flow, Turbulence and Combustion 2016 98:3*, vol. 98, no. 3, pp. 887–922, Nov. 2016, doi: 10.1007/S10494-016-9777-7.

[9] P. Glarborg, J. A. Miller, B. Ruscic, and S. J. Klippenstein, "Modeling nitrogen chemistry in combustion," *Prog. Energy Combust. Sci.*, vol. 67, pp. 31–68, Jul. 2018, doi: 10.1016/J.PECS.2018.01.002.

[10] B. M. Pinto, G. P. Pacheco, M. A. A. Mendes, and P. J. Coelho, "Numerical Simulation of Natural Gas/Hydrogen Combustion in a Novel Laboratory Combustor," *Applied Sciences 2025, Vol. 15, Page 7123*, vol. 15, no. 13, p. 7123, Jun. 2025, doi: 10.3390/APP15137123.

[11] B. Aravind, S. Sadasivam, J. Davies, S. Mashruk, and A. Valera-Medina, "Experimental demonstration of in-situ cracked premixed swirl NH3-air flames," *Appl. Energy*, vol. 401, p. 126754, Dec. 2025, doi: 10.1016/J.APENERGY.2025.126754.

[12] A. Valera-Medina *et al.*, "Ammonia–methane combustion in tangential swirl burners for gas turbine power generation," *Appl. Energy*, vol. 185, pp. 1362–1371, Jan. 2017, doi: 10.1016/J.APENERGY.2016.02.073.

[13] A. Valera-Medina, D. G. Pugh, P. Marsh, G. Bulat, and P. Bowen, "Preliminary study on lean premixed combustion of ammonia-hydrogen for swirling gas turbine combustors," *Int. J. Hydrogen Energy*, vol. 42, no. 38, pp. 24495–24503, Sep. 2017, doi: 10.1016/J.IJHYDENE.2017.08.028.

[14] A. Valera-Medina *et al.*, "Premixed ammonia/hydrogen swirl combustion under rich fuel conditions for gas turbines operation," *Int. J. Hydrogen Energy*, vol. 44, no. 16, pp. 8615–8626, Mar. 2019, doi: 10.1016/J.IJHYDENE.2019.02.041.

[15] D. Füzesi, S. Wang, V. Józsa, and C. T. Chong, "Ammonia-methane combustion in a swirl burner: Experimental analysis and numerical modeling with Flamelet Generated Manifold model," *Fuel*, vol. 341, p. 127403, Jun. 2023, doi: 10.1016/J.FUEL.2023.127403.

[16] R. De Robbio, "Innovative combustion analysis of a micro-gas turbine burner supplied with hydrogen-natural gas mixtures," *Energy Procedia*, vol. 126, pp. 858–866, Sep. 2017, doi: 10.1016/J.EGYPRO.2017.08.291.

[17] S. Taamallah, K. Vogiatzaki, F. M. Alzahrani, E. M. A. Mokheimer, M. A. Habib, and A. F. Ghoniem, "Fuel flexibility, stability and emissions in premixed

hydrogen-rich gas turbine combustion: Technology, fundamentals, and numerical simulations," *Appl. Energy*, vol. 154, pp. 1020–1047, Sep. 2015, doi: 10.1016/J.APENERGY.2015.04.044.

[18] J. Nam and J. J. Yoh, "A numerical investigation of the effects of hydrogen addition on combustion instability inside a partially-premixed swirl combustor," *Appl. Therm. Eng.*, vol. 176, p. 115478, Jul. 2020, doi: 10.1016/J.APPLTHERMALENG.2020.115478.

[19] A. A. Khateeb, T. F. Guiberti, X. Zhu, M. Younes, A. Jamal, and W. L. Roberts, "Stability limits and NO emissions of technically-premixed ammonia-hydrogen-nitrogen-air swirl flames," *Int. J. Hydrogen Energy*, vol. 45, no. 41, pp. 22008–22018, Aug. 2020, doi: 10.1016/J.IJHYDENE.2020.05.236.

[20] Z. Li and S. Li, "Kinetics modeling of NOx emissions characteristics of a NH3/H2 fueled gas turbine combustor," *Int. J. Hydrogen Energy*, vol. 46, no. 5, pp. 4526–4537, Jan. 2021, doi: 10.1016/J.IJHYDENE.2020.11.024.

[21] K. Zhang, Y. Z. Shen, R. Palulli, A. Ghobadian, J. Nouri, and C. Duwig, "Combustion characteristics of steam-diluted decomposed ammonia in multiple-nozzle direct injection burner," *Int. J. Hydrogen Energy*, vol. 48, no. 42, pp. 16083–16099, May 2023, doi: 10.1016/J.IJHYDENE.2023.01.091.

[22] S. Karyeyen, J. S. Feser, and A. K. Gupta, "Swirl assisted distributed combustion behavior using hydrogen-rich gaseous fuels," *Appl. Energy*, vol. 251, p. 113354, Oct. 2019, doi: 10.1016/J.APENERGY.2019.113354.

[23] P. W. Agostinelli, D. Laera, I. Chterev, I. Boxx, L. Gicquel, and T. Poinsot, "On the impact of H2-enrichment on flame structure and combustion dynamics of a lean partially-premixed turbulent swirling flame," *Combust. Flame*, vol. 241, p. 112120, Jul. 2022, doi: 10.1016/J.COMBUSTFLAME.2022.112120.

[24] X. Wei, M. Zhang, J. Wang, and Z. Huang, "Investigation on lean blow-off characteristics and stabilization mechanism of premixed hydrogen enhanced ammonia/air swirl flames in a gas turbine combustor," *Combust. Flame*, vol. 249, p. 112600, Mar. 2023, doi: 10.1016/J.COMBUSTFLAME.2022.112600.

[25] M. Amerighi, A. Andreini, T. Reichel, T. Tanneberger, and C. O. Paschereit, "LES investigation of a swirl stabilized technically premixed hydrogen flame with FGM and TFM models," *Appl. Therm. Eng.*, vol. 247, p. 122944, Jun. 2024, doi: 10.1016/J.APPLTHERMALENG.2024.122944.

[26] P. Weigand, W. Meier, X. R. Duan, W. Stricker, and M. Aigner, "Investigations of swirl flames in a gas turbine model combustor: I. Flow field, structures, temperature, and species distributions," *Combust. Flame*, vol. 144, no. 1–2, pp. 205–224, Jan. 2006, doi: 10.1016/J.COMBUSTFLAME.2005.07.010.

[27] W. Meier, X. R. Duan, and P. Weigand, "Investigations of swirl flames in a gas turbine model combustor: II. Turbulence–chemistry interactions," *Combust. Flame*, vol. 144, no. 1–2, pp. 225–236, Jan. 2006, doi: 10.1016/J.COMBUSTFLAME.2005.07.009.